Review Article

Experimental Investigation and Simulation of Electro-Mechanical Behavior of Hybrid Sandwich Composite Radomes for Aerospace Applications

Zhaib Muneer Ahmed [a] , Muhammad Ali Nasir [a] ,
Zafar Iqbal [b*] Muhammad Talha Aamir [a]

[a] *Department of Mechanical Engineering, University of Engineering & Technology (UET) Taxila, Rawalpindi, Punjab 47050, Pakistan*
[b] *School of Chemical & Materials Engineering (SCME), National University of Science & Technology (NUST) Islamabad, Pakistan*

ARTICLE INFO

ABSTRACT

This paper presents a comprehensive study of the material selection, manufacturing, and Electro-Mechanical testing of radomes made from Polymer Matrix Sandwich Composite materials. The objective is to achieve optimal electromagnetic (EM) and mechanical performance using a combination of PMI foam core and hybrid face sheets (Kevlar & S Glass) sandwich composite structures. The selection of the material configuration was based on a Multi Criteria Decision Matrix (MCDM) method to meet the requirements of Electromagnetic Interference (EMI) transparency and aerodynamic/inertial loads during flights. A full-scale nose radome was manufactured using a hand-layup technique assisted by vacuum bagging, specifically designed for flight vehicles with speeds up to <0.8 Mach. The EMI behavior of the radome was experimentally tested using the free space measurement method and verified through numerical modeling in Altair FEKO software, which showed minimal EM losses of 3% and <1% respectively. Multiple specimens were prepared to determine the mechanical properties and were tested according to ASTM standards for tensile and flexural properties. Additionally, finite element modeling (FE) was employed to validate the mechanical properties of the radome, ensuring that it meets the required constraints. The combined results from the EMI testing, FE modeling, and mechanical testing provided an optimum combination of materials and structure that satisfies the functional requirements of the radome.

1. Introduction

Aerospace vehicles are equipped with radomes to shield radar systems from operational and environmental stresses that may disrupt the electromagnetic (EM) wave patterns of the radar antenna [1]. The ideal radome material should possess both transparency to EM energy and structural integrity to withstand operational loads [2-5]. While there is a plethora of material options available for sandwich structures, the choices for radome construction are relatively limited [6]. A highly effective approach for achieving desirable properties is through the hybridization of composites, as evidenced by numerous studies in the literature on polymer composites. E/S-Glass and Aramid composites, known for their minimal interference with EM wave transmission, are commonly employed in the construction of radomes, often configured as sandwich structures [7].

However, it's important to note that E-glass/epoxy and aramid/epoxy composites possess distinct EM and mechanical properties [7,8]. Consequently, combining these materials as a hybrid composite face for a radome allows for more efficient utilization of their strengths [7,8]. Moreover, there has been a recent surge of interest in sandwich structures incorporating foam cores [9]. These structures are favored due to their excellent crush resistance [10], lightweight characteristics [11], and exceptional energy absorption capabilities [12]. The two critical material properties determining radome functionality are the dielectric constant (εr), which regulates the reflection of electromagnetic signals, and the dielectric loss tangent (tan δ), governing the absorption of electromagnetic signals as they pass through the radome's surface (thickness) [13–15].

A research project was proposed to design and assess a hybrid composite low-observable radome suitable for X-band frequency applications. This endeavor incorporated using both E-glass/epoxy and aramid/epoxy composites as the hybrid composite face to harness their distinct properties selectively [16]. To gain valuable insights into the impact of radomes on antenna performance, an extensive analysis was conducted using the FEKO software [17]. This study encompassed a series of simulations involving various types of composite radomes, including those with honeycomb and foam cores, and assessed their influence on the electromagnetic properties of antennas [18]. The authors meticulously compared their simulation outcomes with experimental data, affirming the precision and efficacy of the Finite Difference Time Domain (FDTD) method in conjunction with the FEKO software.

In addition, a numerical analysis was conducted on composite sandwich radomes utilizing the FEKO software. This investigation sought to explore the effects of various design parameters on the electromagnetic performance of the radomes [19]. The simulation results underscored the significance of outer skin thickness and core material thickness in determining radome performance. It was observed that increasing the thickness of the core material yielded improvements in radome performance, as it led to a reduction in transmission loss and an enhancement in directivity.

In the present study, the focus is on the utilization of Kevlar-Foam-Glass hybrid sandwich composites in nose radomes (Fig. 1), a choice made to effectively address specific design requirements. For enhanced resistance to moisture and protection against ultraviolet (UV) radiation, S-Glass face sheets are employed on the outer surface. Simultaneously, Kevlar face sheets are selected for their ability to impart strength, toughness, and structural integrity to the radome. The foam core material is strategically chosen to exhibit in-phase properties

concerning electromagnetic (EM) radiation. The optimization of radome wall thickness is conducted with a keen consideration of the dielectric properties inherent in the employed materials.

To comprehensively assess the performance of these composite structures, mechanical characterization was carried out, encompassing various tests such as tensile, flexural, and inter-laminar shear strength (ILSS) tests. These experimental findings are further validated through finite element (FE) modeling techniques. The electromagnetic (EM) analysis involved the experimental testing of a full-scale radome within an EM chamber, and these empirical observations are substantiated through numerical simulations conducted using the FEKO software. The outcome of this extensive analysis serves to provide invaluable insights into both the mechanical and EM characteristics of the selected nose radome materials, facilitating a deeper understanding of their performance and suitability for the intended applications.
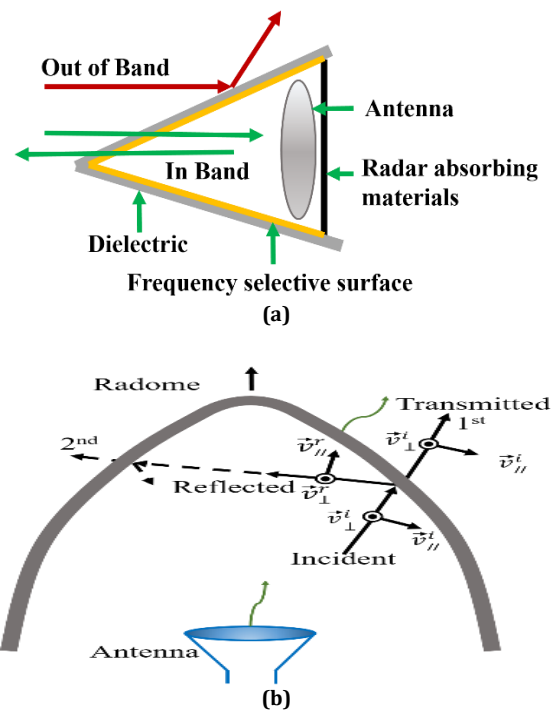

Fig. 1. (a), (b) Schematic Representation of Nose Radome [20]

2. Material Selection and Fabrication of Full-Scale Radome

The material selected for the fabrication of the nose radome is based on the Multi Criteria Decision Matrix (MCDM).

2.1. Material Selection (MCDM)

Multi-criteria decision-making (MCDM) is a well-structured, multidimensional quantitative and qualitative procedure designed to address decision-

making issues in various domains. In this research, MCDM has been employed to optimally select the appropriate materials for aircraft nose radome that must offer sufficient mechanical properties as well as low dielectric constants. Since different MCDM techniques have been suggested in the literature, three types of techniques i.e. TOPSIS, PROMETHEE II, and VIKOR were selected for the current research work. While carrying out calculations for all three techniques (TOPSIS, PROMETHEE II, and VIKOR), the most suitable electro-mechanical properties were selected keeping in consideration the application requirements. The values of weightage were assigned to each property by their significance in the structural, aerodynamic, and electromagnetic performance required from the radome. Percentage weightage of fiber materials and their associated properties are tabulated in Table 1.

Table 1. MCDM Criterion and Weights

Weightage	0.2	0.15	0.25	0.3	0.1
Attribute / Criteria	Tensile Strength	Density	Fracture Toughness	Dielectric Constant	Cost
Alternatives	GPa	g/cm^3	MPa. m$^{0.5}$	-	USD/Kg
E-Glass	1.95	2.55	0.5	6.13	1.63
S-Glass	4.7	2.49	0.5	4.5	19.6
Kevlar 49	2.5	1.44	2	4.1	70.3
Kevlar 29	2.9	1.43	2	4.2	24.5
Carbon	2.3	2.05	1	8	134

Fig. 2. Nose Radome

In this research project, five different fiber materials were selected as face sheets in the composite sandwich structure. These materials are referred to as 'alternatives,' and their specific properties are categorized as 'attributes' or 'criteria,' as detailed in Table 1. Subsequently, all three evaluation techniques were applied to establish rankings for these candidate materials based on the specified criteria, as summarized in Table 2.

Table 2. Ranking of Materials through MCDM Techniques

Alternatives	Ranking of materials		
	TOPSIS	PROMETHEE II	VIKOR
E-Glass	2	4	4
S-Glass	1	3	3
Kevlar 49	3	2	2
Kevlar 29	4	1	1
Carbon	5	5	5

Kevlar 29 was found at 1st rank in PROMETHEE II and VIKOR MCDM techniques, however, it was ranked 4th in TOPSIS. Kevlar 49 obtained 2nd rank both in PROMETHEE II and VIKOR, while ranked 3rd in TOPSIS. S-glass was ranked 1st in TOPSIS and remained at 3rd rank in PROMETHEE II and VIKOR. Based on the overall rankings, S Glass and Kevlar 49 were finally selected for the construction of the radome as shown in Fig 2. S-glass was selected for outer face sheets because of its additional performance in moisture absorption and UV protection and Kevlar 49 for inner face sheet for better impact resistance and fatigue properties.
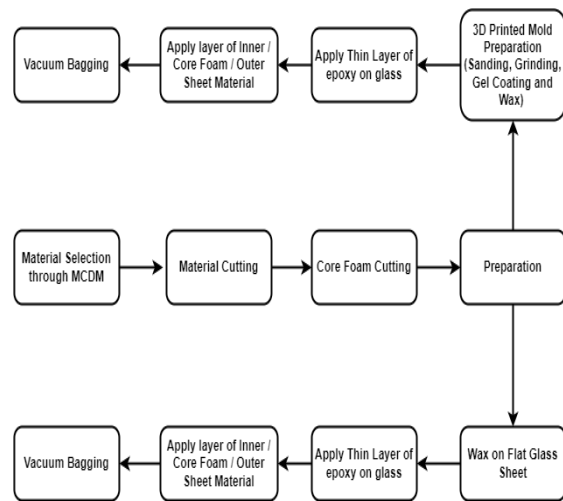

Fig. 3. Radome Manufacturing Flow Chart

Table 3. Woven Fabric Properties

Property	Aramid	S-Glass
Weave Pattern	Plain Weave	Plain Weave
Area density (g/m²)	200	200
Thickness (mm)	0.25	0.2
Rows per inch	12	16

2.2. Fabrication Process

For this research, plain weave Kevlar 49 and S Glass Fibres were purchased from Wuxi GDE Technology Co., Ltd, and Jiangsu Mingchen Equipment Co., Ltd respectively (Table 3). The radome was fabricated (Fig. 3) using a low viscous, clear, epoxy liquid resin by RIAERO Italy, the properties of which are tabulated in Table 4. Polymethacrylimide (PMI) Foam (Rohacell, HF51, EVONIK, Germany) was selected due to better dielectric properties. The resin and hardener were uniformly mixed in a ratio of 2:1 by weight percentage. The Radome was fabricated in sandwich configurations with three layers each of Kevlar and S Glass on either side of 4 mm thick PMI foam. The average thickness of each layer was 0.2 mm with the total thickness of the Sandwich Structure <6 mm. After curing, a fiber volume fraction of 60 % was achieved.

Table 4. Properties of Liquid Epoxy Resin

Property	Values
Appearance	Clear
Viscosity at 25°C (MPa)	1200–1800
Density at 25°C (g/cm³)	0.9–0.95
Tensile Strength (MPa)	70–80
Flexural Strength (MPa)	103–117

2.3. Mechanical Testing of Radome Materials

For this study, the mechanical behavior of selected sandwich composites was investigated in systematic experimental procedures. Test specimens were fabricated and cut from the laminate plates in rectangular beams using a jigsaw cutter

2.3.1. Tensile Testing

The tensile testing of the composite specimen was performed on a universal testing machine (Zwick Roewell Z100), according to the ASTM D3039 standard, using a crosshead speed of 2 mm/min and a 100 kN load cell. Specimens were cut from the prepared laminate composite panels. The composite specimens of nominal dimension 250 × 25 × 2.5 mm (Length x width x thickness) were used for the tensile testing (Fig. 4).

Fig. 4. Tensile Testing

2.3.2. Flexural Testing

The flexural strength and modulus of the composite specimens were determined using the three-point bend test method following the ASTM D7264 standard. This test was performed on the Jinan Zhongzhang Universal testing machine with a 10 kN load cell. The load was placed midway between the supports. The crosshead speed applied was 3 mm/min.

The bending strength was calculated using the following equation.

$$\sigma = \frac{3F_{max}L}{2bh^2} \tag{1}$$

where, b, h, and L are the width, height, and length respectively of the composite specimen used and Fmax is the maximum load.

2.3.3. Inter Laminar Shear Strength Testing (ILSS)

The inter-laminar shear strength test was performed on composite specimens using the ASTM D2344 standard. This test was performed on the Jinan Zhongzhang Universal testing machine with a 10 kN load cell. The specimen of size 40 × 12 × 4 mm was used to conduct a short beam shear test (Fig. 5) under the three-point bending with a 10 mm span at a crosshead speed of 1 mm/min using the same testing machine as for the flexural test. The inter-laminar shear strength (ILSS) was found using Equation (2).

$$\tau = \frac{3F_{max}}{4wd} \tag{2}$$

where, w and d, are the width and depth, respectively, of the composite specimen used and Fmax is the maximum load. The results of the tests are given in Table 5.
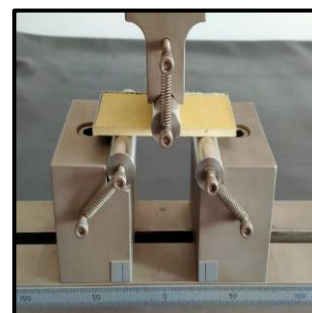

Fig. 5. Short Beam Shear Testing

Table 5. Results of Mechanical Testing

Testing	Material	Sample 1	Sample 2	Sample 3	Mean
Tensile Strength (MPa)	S Glass	273	260	245	259
	Kevlar49	349	335	321	335
Flexural Strength (MPa)	S Glass	394	357	346	365
	Kevlar49	354	321	304	326
ILSS (MPa)	S Glass	18	22	23	20
	Kevlar49	25	24	26	25

3. Finite Element (FE) Modelling

The structural analysis of the radome was performed in the Ansys static structural module. The Ansys Composite PrePost (ACP) module was utilized to develop an initial model of the composite structure, which includes defining its geometry, material properties, and layup. Subsequently, this composite model was transferred to a static structure module for static analysis to assess its strength and durability by calculating the factor of safety against the stresses. The data obtained from the static module was then transferred to an eigenvalue-buckling module to determine the value of the buckling factor. The radome structural model was composed of 2D shell elements with laminate composite properties as its definitions. The Roha cell foam core was modeled as isotropic, while the S-glass and Kevlar-49 plies were modeled as orthotropic material with young modulus $E_x=E_y$ and $E_z=0$. Nodes at the base of the nose cone were restricted in all degrees of freedom to depict the connection between the radome and fuselage.

3.1. Meshing and Analysis Setup

To calculate the radome deformations under aerodynamic and inertial loads at various flight conditions such as takeoff, landing, climb, nose dive, and emergency landing scenarios the pressure profiles obtained from the Computational Fluid Dynamics (CFD) analysis were mapped onto the structural Finite Element Analysis (FEA) model. The model was meshed using structural quad elements with a mesh element size of 2mm. The meshed model, boundary conditions, and loading conditions are shown in Fig 6 (a) & (b) respectively.
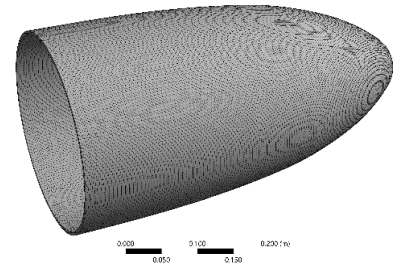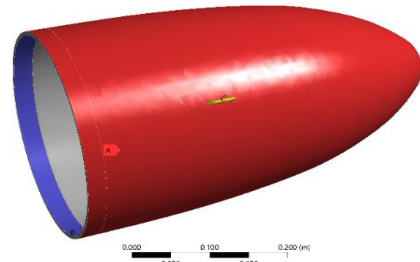

Fig. 6 (a). Meshing on Radome

Fig. 6 (b). Boundary Conditions & Loading

3.2. Results and Discussions (FE Analysis)

Figures 7(a) & 7(b) illustrate the von Mises stresses in the skin plies and foam core of the radome structure under the given loading conditions of a speed of 0.8 Mach and 4.5 G's of inertial load. These figures offer important insight into the stress distribution and potential areas of concern in the radome structure.
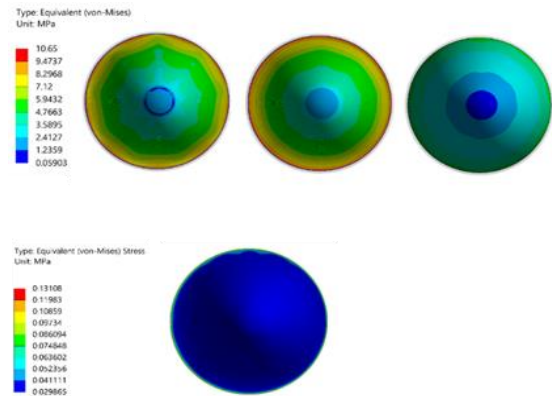

Fig. 7 (a). Von-Mises stresses on outer S Glass face sheet plies and foam core (Front View)
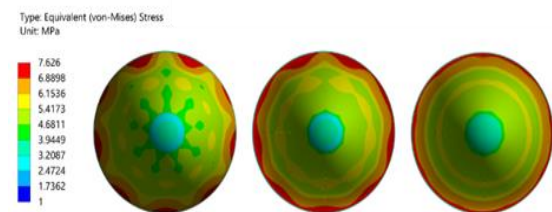

Fig. 7 (b). von-Mises stresses on inner Kevlar face sheet plies (Front View)

In addition, Figure 8(a) illustrates the amount of deformation that the radome structure experiences under these loading conditions, providing valuable information on how the structure responds to the applied loads. Figure 8(b) depicts the Eigen-value bulking, which indicates the structure's resistance to buckling under these conditions. Both of these figures offer a clear visual representation of the radome's structural performance and can help in the design and optimization of the structure to ensure its reliability and safety.
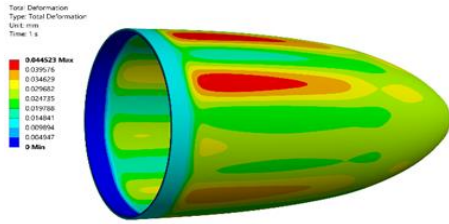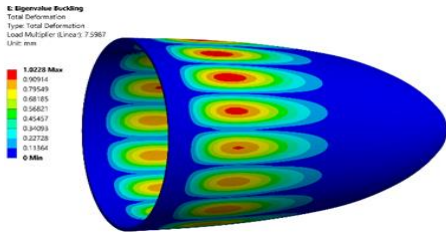

Fig. 8 (a). Total deformation of radome structure

Fig. 8 (b). Eigen-value bulking of radome structure

Table 6. Results from ANSYS WORKBENCH

Layup Sequence	Thickness (mm)		Total Deformation (mm)	Failure Criteria		Von-Mises Stress (MPa)
	Face Sheets	Core		Tsai-Wu	Bulking Factor	
3G-F-3K	2.0	4.0	0.044	23.07	7.59	10.65

The results presented in Table 6 depict the FEA results of the sandwich structure which is comprised of three layers each of 0.2mm S-Glass as the outer face sheet and three layers of 0.2mm Kevlar as the inner face sheet with a 4 mm PMI core. It is revealed that under given operating conditions the maximum stress experienced by the structure is 10.65 MPa whereas, as per the Tasi-Wu criteria this structure can bear a load up to 23.07 MPa. This implies that the sandwich structure is under an FOS of 2.16, which is reasonably good.

4. Electromagnetic Characterization of Radome

To ensure reliable signal transmission, radome walls should be constructed to reduce transmission loss at the operational frequency. The performance of the sandwich panels in terms of electromagnetic wave transmission and reflection was measured using the widely utilized free space test setup.

4.1. Electromagnetic Characteristics of Face Sheet & Core

To perform and validate the EM performance, the following mathematical models were implied

$$E(x, y, 0) = f(x,y)\hat{a}_x + g(x,y)\hat{a}_y \tag{3}$$

where, ax, ay, and az are the unit vectors in the x, y, and z directions respectively.

The plane-wave spectrum associated with each component can be obtained by taking the Fourier transformation of the aperture field components and g as

$$F_x(K_x, K_y) = \iint_A f(x,y)\, exp\{+j(K_x x + K_y y)\}d_x d_y \tag{4}$$

With a similar expression holding for Fy, and if a combined spectrum function F(K) is defined as

$$F(K) = F_x\hat{a}_x + F_y\hat{a}_y + F_z\hat{a}_z \tag{5}$$

where K, the propagation vector is defined as

$$K = K_x\hat{a}_x + K_y\hat{a}_y + K_z\hat{a}_z \tag{6}$$

then

$$F_z = -(K_x F_x + K_y F_y)/K_z \tag{7}$$

With expressions for the field at field point r being

$$E(r) = \int_{-\infty}^{+\infty} \int_{-\infty}^{+\infty} F(K)\exp{(-jk \cdot r)}dk_x\, dk_y \tag{8}$$

and

$$H(r) = \int_{-\infty}^{+\infty} \int_{-\infty}^{+\infty} K^{\wedge}F(K)\exp{(-jk \cdot r)}dk_x\, dk_y \tag{9}$$

4.2. Electromagnetic Simulation of Radome

FEKO software application was used to carry out the EM simulation of radome (Fig. 9) at 8 GHz, 10 GHz, and 12 GHz frequencies, each at three angles of elevation i.e. 0, 15, and 30 degrees.
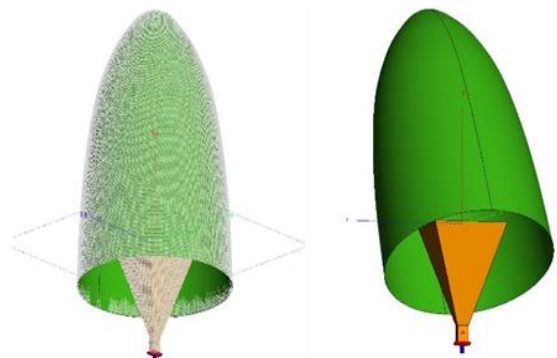

Fig. 9. Meshing and Simulation of Radome on Altair FEKO

Figure 10 illustrates simulations depicting wave patterns of the antenna at frequencies of 8, 10, and 12 GHz. The simulation presents wave patterns both with and without the presence of the radome. The dark blue curve represents the baseline wave pattern without the radome. Additionally, color coding is employed, where the green, red, and sky-blue curves correspond to elevation angles of 0, 15, and 30 degrees, respectively. This color-coded representation facilitates a comprehensive comparison of wave patterns at various angles and frequencies, enabling an assessment of the radome's impact on antenna performance.

At a frequency of 8 GHz (as shown in Figure 10(a)) and an elevation angle of 0 degrees, noticeable side lobes become apparent, accompanied by a gain of -13.492 dB. However, upon the application of the radome at an elevation angle of 15 degrees, the most prominent side lobe exhibits a reduced gain, measuring -17.147 dB. The most substantial reduction in side lobe gain is achieved at an elevation angle of 30 degrees, where the major side lobe reaches an attenuated gain of -24.4 dB. Crucially, the graph clearly illustrates that the curve at the 30-degree elevation angle closely mirrors the antenna-only curve. This observation strongly suggests that this particular configuration offers optimal performance in terms of elevation for the radome.

The simulation was conducted at a frequency of 10 GHz, as depicted in Figure 10(b), to scrutinize the antenna's wave pattern. At an elevation angle of 0 degrees, prominent side lobes, characterized by a gain of -18.643 dB. At an elevation angle of 15 degrees, the major side lobe exhibits a slightly reduced gain of -18.951 dB. Similarly, at 30 degrees, the major side lobe demonstrates a gain of -24.241 dB. The graph depicts that, at 0 degrees, the wave pattern exhibits pronounced ripples, manifesting as horizontal splines. However, as the elevation increases to 15 and 30 degrees, the ripples persist but become less noticeable. Remarkably, the curve at the 30-degree elevation angle closely mirrors the antenna-only curve. This observation underscores that the configuration at 30 degrees represents the optimal elevation for the radome's performance.

In the simulation performed at a frequency of 12 GHz, as depicted in Figure 10(c), an examination of the antenna's wave pattern with and without the radome reveals significant clarifications. At an elevation angle of 0 degrees, major side lobes manifest, characterized by a gain of -15.193 dB. Upon the application of the radome at an elevation angle of 15 degrees, the major side lobe exhibits a slightly reduced gain of -16.613 dB. Similarly, at an elevation angle of 30 degrees, the major side lobe demonstrates a gain of -23.804 dB. Notably, the curves at 0 and 15 degrees exhibit smooth ripples, signifying a relatively consistent wave pattern. The graph illustrates that, at 30 degrees, the curve closely aligns with the antenna-only curve, signifying that this particular configuration represents the optimal elevation for the radome in the specified scenarios.
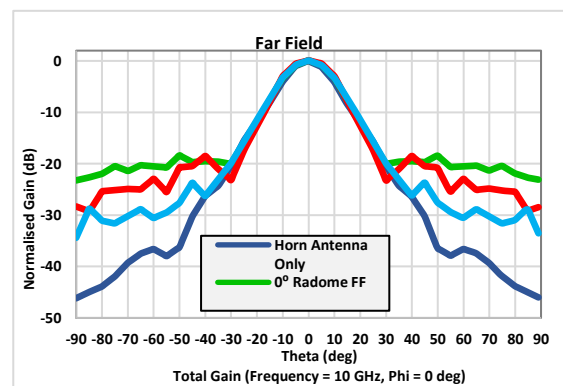

Fig. 10 (a). Antenna pattern @ 8GHz
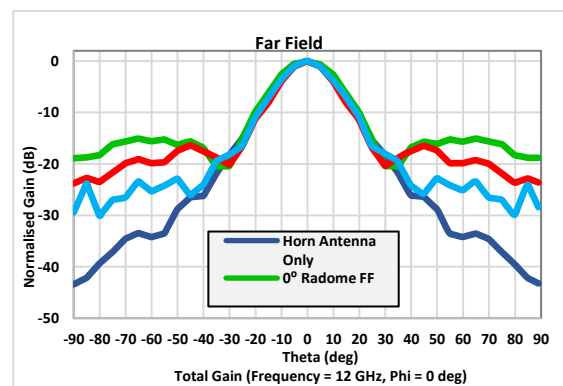
Fig. 10 (b). Antenna pattern @ 10GHz

Fig. 10 (c). Antenna pattern @ 12GHz

Table 7. Side Lobes Level (SLL) at different angles and frequencies (Simulations)

Elevation (deg)	8 Ghz SLL (db)	10 Ghz SLL (db)	12 Ghz SLL (db)
0	-13.49	-18.64	-15.19
15	-17.14	-18.95	-16.61
30	-24.40	-24.24	-23.80

4.3. Results and Discussions (FEKO Simulation)
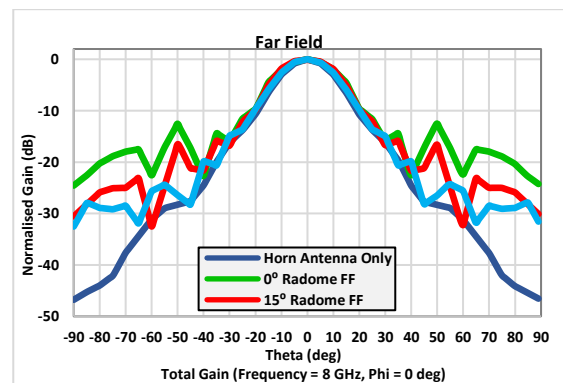
In the simulation results obtained at different frequencies (8 GHz, 10 GHz, and 12 GHz), the performance of the antenna with the radome was compared to the antenna without the radome. The major side lobes and gains were analyzed at different elevation angles (0 degrees, 15 degrees, and 30 degrees) for each frequency. At 8 GHz, the radome at an elevation of 30 degrees showed the closest resemblance to the antenna-only curve, indicating optimal performance in terms of minimizing the impact on side lobes. Similarly, at 10 GHz, the radome at an elevation of 30 degrees exhibited the best performance, with minimal ripples and side lobes, closely resembling the antenna-only curve.

Finally, at 12 GHz, the radome at an elevation of 30 degrees again showed the closest resemblance to the antenna-only curve, indicating the optimal configuration for minimizing the impact on side lobes and maintaining performance. In comparison, the results consistently showed that the radome at an elevation of 30 degrees had the most favorable performance in terms of minimizing side lobes and maintaining the overall wave pattern. This suggests that the selected configuration with the radome at a 30-degree elevation angle provides the best compromise between protecting the antenna and preserving its electromagnetic performance. The results are summarized in Table 7.

These observed variations in antenna wave patterns, both in the presence and absence of the radome, are indicative of a complex interplay of factors. These variations are most notably influenced by the radome's design, material properties, and the specific electromagnetic characteristics inherent to the frequencies of interest, which were 8 GHz, 10 GHz, and 12 GHz. Our analysis suggests that the interaction between the radome and electromagnetic waves is not only frequency-dependent but also heavily reliant on the elevation angle at which the waves strike the radome's surface.

The phenomena observed, such as the emergence of side lobes and the modulation of ripples in the wave patterns, can be attributed to diffraction, interference, and changes in wave propagation introduced by the radome. Furthermore, variations in radome thickness, the choice of dielectric materials, and the overall radome design play pivotal roles in shaping these observed behaviors. To elucidate the underlying mechanisms comprehensively, our research encompasses numerical simulations, sensitivity analyses, and parametric studies, further bolstered by insights from scientific literature and expert consultation. Ultimately, our objective is to unravel the intricate factors contributing to these observations and optimize radome-antenna configurations for optimal performance across diverse operational scenarios.

5. Experimental EM Testing of Full-Scale Radome

To compare and validate results obtained through FEKO simulation, the EM wave pattern behavior of a full-scale radome was tested in an anechoic chamber. The testing utilized a pair of horn antennas (Fig. 11(a)) operating in the X-band frequency range of 8 to 12 GHz. Initially, the wave pattern of the horn antenna without the radome was established as a reference for comparison. Subsequently, the radome was positioned in front of the transmitting antenna (Fig. 11(b)) at three different elevation angles (0 degrees, 15 degrees, and 30 degrees) to observe the antenna's behavior when interacting with the sandwich structure of the radome. By analyzing the wave patterns obtained in both the presence and absence of the radome, the impact of the sandwich structure on the antenna's performance could be evaluated.
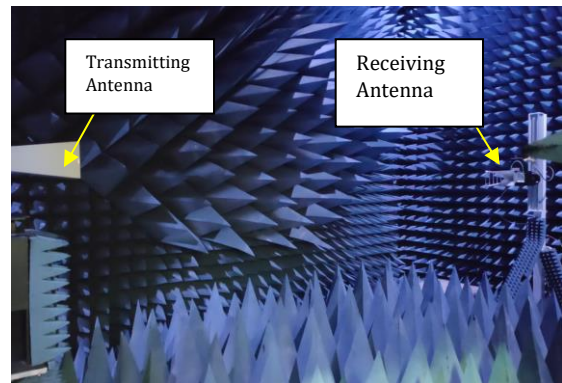

Fig. 11 (a). Anechoic Chamber: Two Horn Antenna, Transmitting and Receiving.
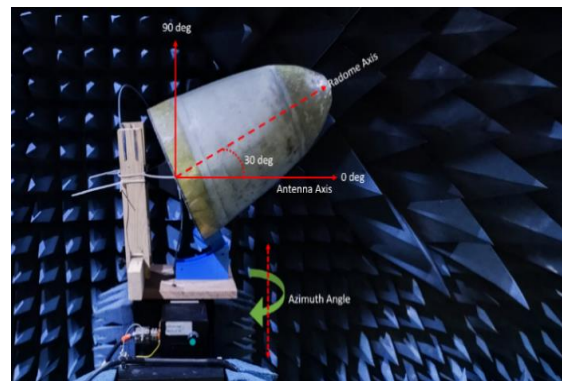

Fig. 11 (b). Radome Setup with Transmitting Antenna in Anechoic Chamber for FAR Field Testing.

The experimental results, as illustrated in Figure 12, provided valuable insights into the wave patterns of the antenna both with and without the presence of the radome. In this visual representation, the baseline wave pattern, devoid of the radome, is depicted by the dark blue curve, serving as a reference for comparison. Elevation angles of 0, 15, and 30 degrees are distinguished by the use of green, red, and sky-blue colors, respectively.

At a frequency of 8 GHz (Figure 12(a)), the experimental findings reveal distinctive features in the wave patterns. Notably, ripples and the emergence of side lobes are observed. The recorded major side lobe levels are -9.8 dB at 0 degrees elevation, -11.4 dB at 15 degrees elevation, and -22.423 dB at 30 degrees elevation. Although similarities in the observed ripples exist across elevations, the wave pattern curve at 30 degrees closely mirrors the original antenna pattern without the radome.

Similarly, at a frequency of 10 GHz (Figure 12(b)), the experimental results highlight the presence of ripples and the formation of side lobes in the wave patterns. Major side lobe levels are measured at -9.38 dB (0 degrees elevation), -12.97 dB (15 degrees elevation), and -25.77 dB (30 degrees elevation). The ripples observed at each elevation exhibit resemblances, and once again, the wave pattern curve at 30 degrees elevation closely emulates the original antenna pattern without the radome.

Experimental testing conducted at a frequency of 12 GHz (Figure 12(c)) also reveals ripples in the wave patterns and the formation of side lobes. The major side lobe levels are recorded as -11.67 dB (0 degrees elevation), -13.36 dB (15 degrees elevation), and -22.50 dB (30 degrees elevation). While some similarities persist in the observed ripples across elevations, the wave pattern curve at the 30-degree elevation configuration closely approximates the original antenna pattern without the radome. These experimental findings provided valuable empirical insights into the interaction between the radome and electromagnetic waves at varying frequencies and elevations.
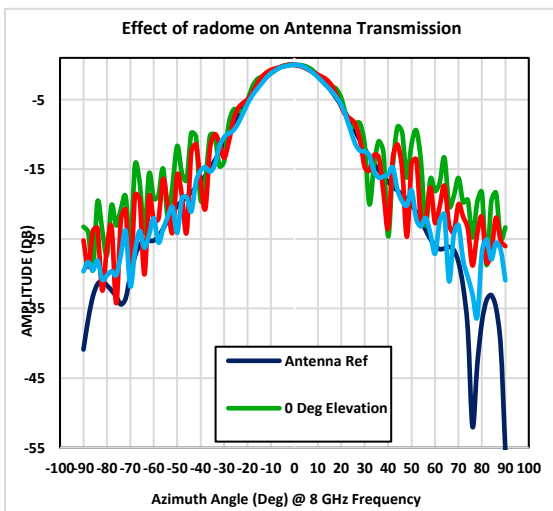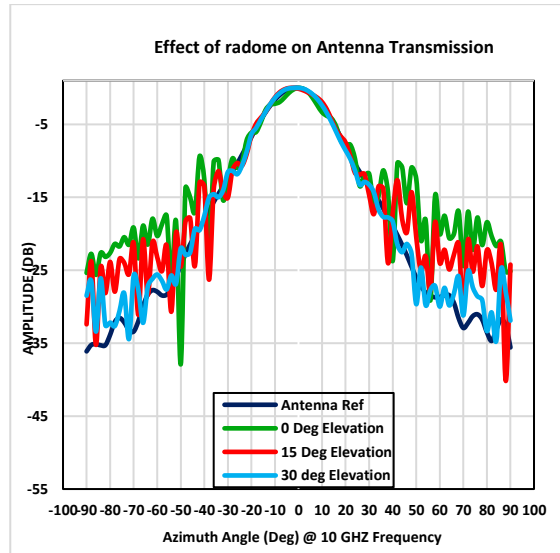

Fig. 12 (b). Antenna pattern @ 10 GHz

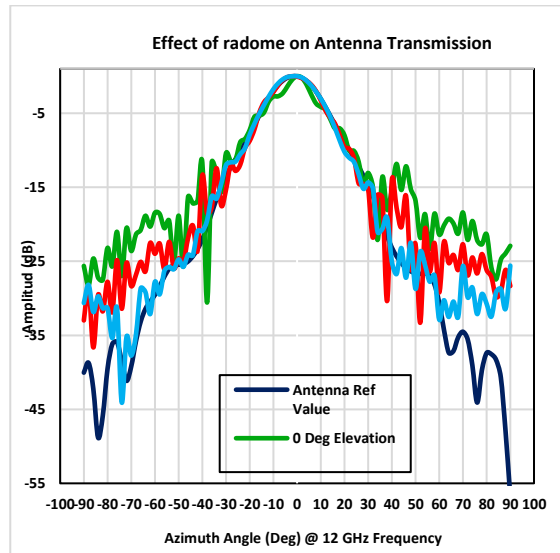**Fig. 12 (c).** Antenna pattern @ 12 GHz

The Results can be summarised and tabulated as

Table 8. Side Lobes Level (SLL) at different angles and frequencies (Experimental)

Elevation (deg)	8 Ghz SLL (db)	10 Ghz SLL (db)	12 Ghz SLL (db)
0	-9.8	-9.38	-11.67
15	-11.4	-12.97	-13.36
30	-22.42	-24.24	-22.50

Fig. 12 (a). Antenna pattern @ 8 GHz

In summary, experimental results (Table 8) across various frequencies (8 GHz, 10 GHz, and 12 GHz) consistently reveal the presence of ripples and the emergence of side lobes in the wave patterns. Notably, the major side lobe levels exhibit variation contingent on the elevation angle, with the 30-degree configuration consistently presenting the closest resemblance to the original antenna pattern, even in the presence of the radome. It's crucial to acknowledge that the experimental testing introduces additional noise and distortions, primarily stemming from manufacturing imperfections associated with the hand lay-up technique employed in radome construction. These findings underscore the significant influence of the radome on wave patterns and underscore the critical importance of carefully selecting the appropriate elevation angle to achieve optimal performance while mitigating undesirable effects arising from manufacturing realities.

6. Results and Discussions

The numerical results, obtained through simulations at different frequencies (8 GHz, 10 GHz, and 12 GHz), have provided critical insights into the performance of the antenna with and without the radome. These insights were complemented and further substantiated by the experimental findings, which focused on the same frequency range and elevation angles (0 degrees, 15 degrees, and 30 degrees). In numerical simulations, it was observed that the radome at an elevation of 30 degrees consistently demonstrated the closest resemblance to the antenna-only curve, indicating optimal performance in terms of minimizing side lobes and preserving the overall wave pattern across all tested frequencies. This observation was mirrored in experimental results, where, particularly at 30 degrees elevation, the wave pattern closely approximated the antenna-only curve, despite the presence of ripples and side lobes.

These congruent findings from both numerical simulations and experiments underline the robustness of the radome's performance at a 30-degree elevation angle. This configuration strikes a balance between the protection of the antenna while maintaining its electromagnetic performance. The observed variations in wave patterns, although complex, can be attributed to factors such as diffraction, interference, and changes in wave propagation introduced by the radome, as well as variations in radome thicknesses and material properties.

In essence, this combined numerical and experimental analysis leads to the conclusion that for the specified frequencies of interest (8 GHz, 10 GHz, and 12 GHz), the radome positioned at a 30-degree elevation angle offers the most favorable compromise between safeguarding the antenna and preserving its electromagnetic functionality. These findings are crucial for optimizing radome-antenna configurations across a range of operational scenarios.

The enhanced performance of the radome-antenna configuration at a 30-degree elevation angle can be attributed to several interconnected factors. At lower elevation angles, electromagnetic waves impinge upon the radome's surface at steeper angles, leading to more pronounced diffraction and interference effects, which manifest as side lobes and ripples in the wave pattern. However, at the 30-degree elevation angle, the incidence angle becomes shallower, reducing the influence of these disturbances. Additionally, electromagnetic waves at this angle exhibit smoother propagation through the radome, resulting in a cleaner wave pattern that closely mirrors the antenna-only curve. This specific angle represents a strategic compromise between safeguarding the antenna from environmental factors and physical damage while minimizing disruptions to electromagnetic wave propagation. The observed reduction in side lobe levels at 30 degrees indicates that the radome causes fewer reflections and scatterings of the waves, contributing to the overall improved performance. In essence, the 30-degree elevation angle serves as an optimal configuration that balances protection and performance, making it ideal for diverse operational scenarios.

7. Conclusions

In conclusion, the presented study on the interaction between radomes and antenna wave patterns has provided valuable insights into the performance of radome-antenna configurations across a spectrum of frequencies (8 GHz, 10 GHz, and 12 GHz) and elevation angles (0 degrees, 15 degrees, and 30 degrees). Through a combination of numerical simulations and experimental testing, a complex interplay of factors has been revealed that significantly influence the EM wave patterns.

Numerical results consistently highlight the 30-degree elevation angle as the optimal configuration, closely resembling the original antenna pattern without the radome. This finding emphasizes the critical role of elevation angle selection in minimizing side lobes and preserving overall antenna performance. Experimental findings, while aligning with the numerical results, introduce a practical dimension to the analysis. The experimental testing introduces additional noise and distortions, primarily stemming from manufacturing imperfections inherent in the hand lay-up technique employed in radome construction. Incorporating numerical and experimental insights, the presence of ripples and side lobes in wave patterns is a complex phenomenon influenced by various factors, including diffraction, interference, changes in wave

propagation introduced due to variations in radome thickness, and material properties.

In light of these findings, it becomes evident that achieving optimal performance is a delicate compromise between protecting the antenna from environmental factors / physical damages while minimizing disruptions to electromagnetic wave propagation. The 30-degree elevation angle consistently offers this balance across various frequencies, making it the preferred configuration for practical radome-antenna setups. However, the comparison between numerical and experimental results underscores the importance of addressing manufacturing imperfections in radome construction. The experimental setup introduced noise and distortions primarily due to these imperfections, which were not as pronounced in the numerical simulations. Therefore, refining manufacturing techniques to reduce such imperfections is crucial to ensuring the reliability and effectiveness of radome-antenna systems.

Conflicts of Interest

The authors declare that there is no conflict of interest regarding the publication of this article.

References

[1] Lansink Rotgerink, Jesper & van der Ven, Harmen & Voigt, T. & Jehamy, E. & Schick, M. & Schippers, H., 2016. Modelling of effects of nose radomes on radar antenna performance. 1-5. 10.1109/EuCAP.2016.7481773.

[2] Zhou, Licheng & Pei, Yongmao & Fang, Daining., 2015. Dual-Band A-Sandwich Radome Design for Airborne Applications. *IEEE Antennas and Wireless Propagation Letters,* 15. 1-1. 10.1109/LAWP.2015.2438552.

[3] Denish Davis, Francis Mathew, Jamaludheen. K.P, N. Seenivasaraja, Karthikeyan. A., 2015. Design and Analysis of Different Types of Aircraft Radome. *INTERNATIONAL JOURNAL OF ENGINEERING RESEARCH & TECHNOLOGY (IJERT) NCRAIME, 2015,* (Volume 3 – Issue 26).

[4] Bhowmik, S., 2017. Investigation of Wide Band mm-Wave Radome. *Dissertation*.

[5] Kraus, J.D. and Marhefka, R.J., 2002. Antennas for all Applications. *McGraw-Hill, New York.*

[6] Castanie, B., Bouvet, C. and Ginot, M., 2020. Review of composite sandwich structure in aeronautic applications. *Composites Part C: Open Access*, *1*, p.100004.

[7] Khatavkar, N. and Balasubramanian, K., 2016. Composite materials for supersonic aircraft radomes with ameliorated radio frequency transmission-a review. *RSC advances*, *6*(8), pp.6709-6718.

[8] Kozakoff, D.J., 2010. *Analysis of Radome-enclosed Antennas*. Artech House.

[9] Fathi, A., Wolff-Fabris, F., Altstädt, V. and Gätzi, R., 2013. An investigation on the flexural properties of balsa and polymer foam core sandwich structures: Influence of core type and contour finishing options. *Journal of Sandwich Structures & Materials*, *15*(5), pp.487-508. 10.1177/1099636213487004.

[10] Siriruk, A., Weitsman, Y.J. and Penumadu, D., 2009. Polymeric foams and sandwich composites: Material properties, environmental effects, and shear-lag modeling. *Composites Science and Technology*, *69*(6), pp.814-820. 10.1016/j.compscitech.2008.02.034.

[11] Ren, P., Tao, Q., Yin, L., Ma, Y., Wu, J., Zhao, W., Mu, Z., Guo, Z. and Zhao, Z., 2020. High-velocity impact response of metallic sandwich structures with PVC foam core. *International Journal of Impact Engineering*, *144*, p.103657.

[12] Al-Shamary, A.K.J., Karakuzu, R. and Özdemir, O., 2016. Low-velocity impact response of sandwich composites with different foam core configurations. *Journal of Sandwich Structures & Materials*, *18*(6), pp.754-768.

[13] Ashby, Michael F., 2011. Chapter 6 - Case Studies: Materials Selection, Editor(s): Ashby, Michael F., Materials Selection in Mechanical Design (Fourth Edition), Pages 125-195, https://doi.org/10.1016/B978-1-85617-663-7.00006-0.

[14] Tricoles, G.P., 1988. Radome Electromagnetic Design, Springer Science, New York, pp. 2051–2081, Chapter 31, Antenna Handbook. https://doi.org/10.1007/978-1-4615-6459-1-31.

[15] Audone, B., Delogu, A. and Moriondo, P., 1988. Radome design and measurements. *IEEE Transactions on Instrumentation and measurement*, *37*(2), pp.292-295. https://doi.org/10.1109/ 19.6069.

[16] Choi, I. and Lee, D., 2014. Hybrid composite low-observable radome composed of E-glass/aramid/epoxy composite sandwich construction and frequency selective surface. *Composite Structures*, *117*, pp.98-104. doi: https://doi.org/10.1016/j.compstruct.2014.06.031.

[17] Almajali, E., McNamara, D. and Lee, D., 2010, July. Using electromagnetic simulation code FEKO as a numerical laboratory in antenna engineering. In 2010 14th International Symposium on Antenna Technology and Applied Electromagnetics & the American Electromagnetics Conference, Ottawa, Canada, (pp.1-4). IEEE. doi: 10.1109/ANTEM.2010.5552545.

[18] Saraiva, E.A., Souza, M.F., Tertuliano Filho, H., Junior, W.A., Benetti, C.A. and Dartora, C.A., 2006, May. The FDTD Simulating the Attenuation of a Plan Electromagnetic Wave Crossing of a Radome in the Weather Radar. In 2006 International Radar Symposium, Krakow, Poland, pp. 1-6, doi: 10.1109/IRS.2006.4338152.

[19] Radomes, M. S., Efficient Design and Analysis of Airborne Radomes. *Channels*, 4, p.5G.

[20] Meng, H. and Dou, W., 2010. Analysis and Design of Radome in Millimeter Wave Band. INTECH Open Access Publisher.